JOURNAL OF GEOPHYSICAL RESEARCH, VOL. 102, NO. B4, PAGES 8313–8327, APRIL 10, 1997

Mantle discontinuity structure from midpoint stacks of converted P to S waves across the Yellowstone hotspot track

Kenneth G. Dueker and Anne F. Sheehan[1]

Cooperative Institute for Research in Environmental Sciences, University of Colorado at Boulder

Abstract. Analysis of a deployment of broadband sensors along a 500-km-long line crossing the Yellowstone hotspot track (YHT) has provided 423 in-plane receiver functions with which to image lateral variations in mantle discontinuity structure. Imaging is accomplished by performing the converted wave equivalent of a common midpoint stack, which significantly improves resolution of mantle discontinuity structure with respect to single-station stacks. Timing corrections are calculated from locally derived tomographic P and S wave velocity images and applied to the Pds (where d is the depth of the conversion) ray set in order to isolate true discontinuity topography. Using the one-dimensional TNA velocity model and a V_p/V_s ratio of 1.82 to map our Pds times to depth, the average depths of the 410- and 660-km discontinuities are 423 and 664 km, respectively, giving an average transition zone thickness of 241 km. Our most robust observation is provided by comparing the stack of all NW back-azimuth arrivals versus all SE back-azimuth arrivals. This shows that the transition zone thickness varies between 261 and 232 km, between the NW and SE portions of our line. More spatially resolved images show that this transition zone thickness variation results from the occurrence of 20-30 km of topography over 200-300 lateral scale lengths on the 410- and 660-km discontinuities. The topography on the 410- and 660-km discontinuities is not correlated either positively or negatively beneath the 600-km-long transect, albeit correlation could be present for wavelengths larger than the length of our transect. If this discontinuity topography is controlled exclusively by thermal effects, then uncorrelated 250° lateral temperature variations are required at the 410- and 660-km discontinuities. However, other sources of discontinuity topography such as the effects of garnet-pyroxene phase transformations, chemical layering, or variations in mantle hydration may contribute. The most obvious correlation between the discontinuity structure and the track of the Yellowstone hotspot is the downward dip of the 410-km discontinuity from 415 km beneath the NW margin of the YHT to 435 km beneath the easternmost extent of Basin and Range faulting. Assuming this topography is thermally controlled, the warmest mantle resides not beneath the Yellowstone hotspot track, but 150 km to the SE along the easternmost edge of the active Basin and Range faulting.

Introduction

For the most part, the radial distribution of seismic velocities and densities of the mantle are controlled by mineralogical variations associated with pressure-induced phase transformations and/or chemical layering. The most seismically visible mineralogic discontinuities are a sequence of phase transformations of olivine to high-pressure forms at the nominal depths of 410 and 660 km producing sharp gradients in the Earth's density and velocity structure [*Bina and Helffrich*, 1994]. The less visible 520-km discontinuity [*Shearer*, 1996] could result from some combination of the β to γ olivine phase transformation and/or transformation of garnet and pyroxene to calcic-perovskite [*Revenaugh and Jordan*, 1991b]. Average magnitudes of the olivine Clapeyron slopes (3 MPa/°C [*Bina and Helffrich*, 1994]) predict that 20 km of equilibrium discontinuity topography at the 410- or 660-km discontinuity requires a temperature anomaly of approximately 250 K. Thus if discontinuity topography is thermally controlled, a coincident velocity anomaly of about 1-2% should be present assuming standard velocity-temperature relations [*Anderson*, 1989]. If the velocity and topographic variations on the olivine phase transitions do not correlate well, then other sources of discontinuity topography are required such as chemical layering and/or discontinuities associated with phase transformation of the garnet/pyroxene component of the mantle [*Anderson*, 1989], hydration effects [*Wood*, 1995], or kinetic effects [*Solomatov and Stevenson*, 1994].

In addition to the well-known olivine phase transitions, a variety of other mantle discontinuities above the 410-km discontinuity have been reported and are of particular interest to understanding the evolution of the upper mantle and its link to lithospheric dynamics. These discontinuities include the Hales, Gutenburg, and Lehmann discontinuities which have been reported in a variety of tectonic regimes [e.g., *Green and Hales*, 1968; *Priestly et al.*, 1994; *Revenaugh and Jordan*, 1991a, b; *Revenaugh and Sipkin*, 1994; *Baumgardt and Alexander*, 1984]. While the interpretation of these shallow discontinuities is debated, proposed origins include the folow-

[1]Also at Department of Geological Sciences, University of Colorado, Boulder.

Paper number 96JB03857.
0148-0227/97/96JB-03857$09.00

ing: partial melting [*Anderson and Sammis*, 1970; *Hales*, 1991], discontinuities in rock fabric [*Leven et al.*, 1981; *Gaherty and Jordan*, 1995], spinel to garnet phase transition [*Hales*, 1969], or chemical layering of eclogitic and peridotitic rocks [*Anderson*, 1989]. Below the 660-km discontinuity, discontinuities have been reported at depths of 720 km [*Revenaugh and Jordan*, 1991b], 920 km [*Kawakatsu and Niu*, 1994; *Stunff et al.*, 1995], and 1200 km [*Stunff et al.*, 1995].

The signals related to mantle discontinuities vary dramatically. Stacks with good event receiver geometries show strong evidence for mantle discontinuity arrivals in some regions and no evidence in other regions [e.g., *Vidale and Benz*, 1992; *Paulssen*, 1988; *Neele and Sneider*, 1992; *van der Lee et al.*, 1994; *Ritsema et al.*, 1995]. Significant signal enhancement by stacking is required to extract energy produced by mantle discontinuities. However, stacking can produce spurious results due to the high levels of signal-generated noise often present at any given station. In addition, incomplete lateral heterogeneity corrections will cause stack incoherence and/or bias discontinuity depth estimates. One way to mitigate the above problems is to collect dense data sets of broadband seismic waveforms from portable deployments and perform the P to S converted wave equivalent of a common midpoint (CMP) stack to form images of the mantle discontinuity structure. This is because an array allows multiple stations to be stacked together so that the signal-generated noise present at a single station becomes incoherent in the multistation stacks. In addition, an array allows creation of well-resolved tomographic velocity models which can be used to accurately correct for lateral velocity heterogeneity [*Saltzer and Humphreys*, 1997; *Schutt et al.*, 1995].

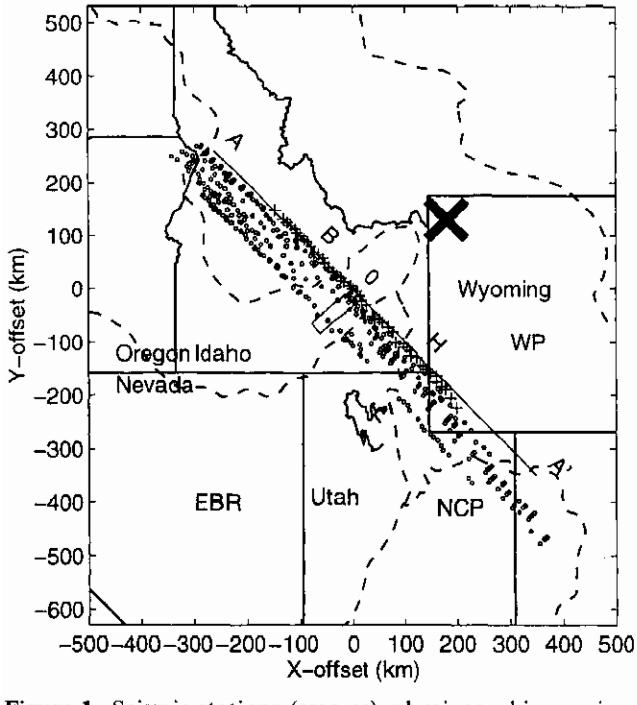

Figure 1. Seismic stations (crosses), physiographic province boundaries (dashed lines), and converted S wave piercing points at 550 km depth (circles). State borders are given by solid lines. Tectonic provinces include WP, Wyoming province; NCP, northern Colorado plateau; EBR, eastern Basin and Range. The Yellowstone caldera is marked by a large cross in NW Wyoming. Line A-A′ is the stacking plane for mantle discontinuity images. YHT, Yellowstone hotspot track; H, hinge line of western U.S. rift margin; B, Borah Peak, highest mountain in Idaho at 13,000 feet. The rectangle shows a sample ray bin; all rays falling within this rectangle are processed together to form a stack trace.

In this paper a two-dimensional cross section of the mantle discontinuity structure across the Yellowstone hotspot track and the late Proterozoic western United States rift margin is presented using broadband data from a recent PASSCAL experiment. We seek to assess any correlation between mantle discontinuity with respect to these tectonic features. The Yellowstone hotspot track (YHT) represents a region of volcanism, extension, and uplift which has propagated about 700 km to the northeast over the last 15 Ma [*Smith and Braile*, 1994]. While a sheared plume origin for the YHT is commonly assumed [e.g., *Smith and Braile*, 1994], the constraints supporting this hypothesis are equivocal. An alternate hypothesis would be that the YHT derives from a local process in which the interplay between extension of the lithosphere over the last 15 Ma [*Rodgers et al.*, 1990] and melt buoyancy driven convective instabilities [*Schmelling and Bussod*, 1996; *Tackley and Stevenson*, 1993] has occurred. Another feature crossed by the seismic array is the "hingeline" of the western U.S. passive margin sedimentary sequence which formed after continental rifting at approximately 700 Ma [*Moores*, 1991]. The hingeline perhaps separates relatively undisturbed ancient continental mantle to the east (i.e., tectosphere [*Jordan*, 1988]) from the "oceanic" mantle which upwelled between the rifting Laurentia supercontinent; thus if this large-scale variation in mantle properties has been preserved, a corresponding variation in the mantle discontinuity structure may be present.

Method

Source Normalization

In this study we analyze data from the 1993 Snake River Plains (SRP) experiment which consisted of the deployment of 20 broadband seismometers (Figure 1). Over the course of the 6-month deployment, each sensor was deployed at two different sites so that a total of 40 sites were occupied. The array was a NW-SE trending line array with an average station spacing of 10-km. Earthquakes at epicentral distances of between 27° and 95° having clear P wave arrivals on both the vertical and radial components were used. Source normalization of the horizontal components is performed by deconvolving the vertical component seismogram from the radial and tangential components [*Langston*, 1977]. The vertical components are windowed by applying a cosine tapered boxcar window from 5 s before to 100 s after the first break of the P wave arrival to the seismograms which extend from 100 s before to 200 s after the P arrival. Because most of the large events are shallow focus, use of a source function of this length is necessary to capture the long interval of incoming P wave energy produced by source side scattering and depth phases. This long source function is valid as long as the majority of the vertical component energy is direct P wave energy arriving at or near the ray parameter of the P wave. The ray parameter of the pP and sP depth phases is negligibly different from the P wave. Secondary phases arriving within our time window with ray parameter values significantly different than P would be PP at distances less than 38° and PcP between 60° and

80°. To avoid this source of error, seismograms with visible *PP* or *PcP* arrivals in these distance ranges are not used. While such a lengthy source function is not an optimal estimate of the converted *S* wave waveform [*Paulssen*, 1988], this approximation only results in a minor degradation of the ability of the deconvolution to "spike" the converted *S* waves. This degradation is more than compensated for by the increased stacking resolution provided by the large increase in useable data. The deconvolution is accomplished by spectral division using a mild water level setting of 0.1 [*Clayton and Wiggins*, 1976] so that the receiver function amplitudes are not greatly affected by the deconvolution. After division, the components of ground motion are inverse Fourier transformed to produce what are commonly called receiver functions [*Langston*, 1977]. In theory, the arrivals present on the radial and tangential receiver functions can be interpreted as *P* to *S* conversions and/or reflections at velocity discontinuities beneath a station. However, in practice a significant fraction of the energy present on receiver functions are not *Pds* arrivals but results from free-surface *P* to *Rg* topographic scattering [*Clauser and Langston*, 1995] and complex *P*-*S* reasonances in sedimentary basins [*Levander and Hill*, 1985].

Ray Tracing and Midpoint Binning

To image spatial variations in the depths to significant velocity discontinuities beneath our array, we geographically bin the ray set. This geographical binning is performed by ray tracing the converted *P* and converted *S* wave ray paths through the one-dimensional TNA reference model to different binning depths (i.e., 50, 250, 400, and 700 km). The tracing is done using the ray parameter of the *P* wave, which is only negligibly different from the ray parameter of our deepest *Pds* arrival (i.e., P660s). After tracing the converted *S* wave ray set downward, the distribution of converted *S* wave ray "piercing points" at a chosen depth (e.g., 200, 400, 700 km depth) is binned. The bins are 75 km wide and spaced every 25 km, which results in a three-bin spatial correlation. Sample bins and the ray coverage are shown in Figure 2, and the piercing points at 700 km depth are shown in Figure 1. Note that all the rays used to form the mantle discontinuity images are within a 80-km-wide swath parallel to our stacking plane (A-A' in Figure 1). This nearly two-dimensional sampling geometry thus minimizes the effects of variable discontinuity structure perpendicular to our array.

Lateral Heterogeneity Corrections

A *Pds* arrival time depends on the differential timing between the *P* and its associated converted *S* wave. Therefore to correct for lateral heterogeneity, timing variations integrated along the two different ray paths associated with a *Pds* arrival must be calculated (Figure 2). The actual *Pds* timing correction applied is the difference between the *S* and *P* correction (Figure 3a). The maximum amplitude of these corrections can be assessed by comparing the teleseismic *P* [*Saltzer and Humphreys*, 1997] and *S* [*Schutt et al.*, 1995] residuals measured from the SRP array. The standard deviation of the 3200 *P* wave and 1100 *S* wave relative residuals is 0.36 and 0.84 s, respectively. To estimate the predicted standard deviation of the *Pds* timing variations, the 623 coincident *P* and *S* source-receiver pairs were identified. To account for the shallower incidence angle of the teleseismic *S* wave with respect to the converted *S* wave, the teleseismic *S* residuals were rescaled to equivalent converted *S* wave times (which reduces the *S* residuals by 13%). Subtraction of the coincident *P* and *S* residuals results in a *Pds* standard deviation of 0.62 s. Thus the *Pds* timing variations imparted by lateral velocity heterogeneity beneath the SRP array are predicted to typically range between ±1.24 s.

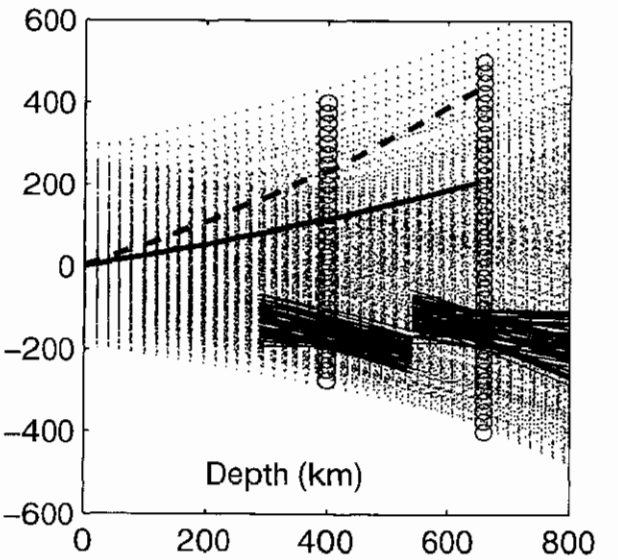

Figure 2. Converted *S* wave ray set. The rays have been traced through our one-dimensional reference model and projected onto the plane beneath the array. The circles at 400 and 700 km depth are bin center points. The rays associated with the binning determined at 400 km are used to form our mantle discontinuity image between 200 and 550 km depth, whereas the binning determined at 700 km is used below 550 km depth. The rays contributing to a few selected bins are shown as solid lines. The ray path of the *P* leg (solid line) and converted *S* leg (dashed line) for a typical *Pds* phase is shown for reference.

To correct for these *Pds* timing variations predicted by the teleseismic residuals, a timing shift is integrated along the *P* and converted *S* wave ray paths through our *P* [*Saltzer and Humphreys*, 1997] and *S* wave [*Schutt et al.*, 1995] tomographic models. Both the *P* and *S* wave models are 400 km deep and achieve a 93% and 82% variance reduction after inversion. The $\partial \ln V_S / \partial \ln V_P$ ratio calculated from the tomographic *S* and *P* models is 2.1, consistent with the slope of the coincident *P* and *S* travel time residuals being 3.4. The simple spatial pattern of the *Pds* timing corrections across the array is shown in Figure 3b. We have chosen to use the tomographic models to correct for the *Pds* timing variations (as opposed to using the teleseismic residuals discussed above) because (1) the tomographic models are of high quality, (2) the converted *S* wave ray path is significantly different from the teleseismic *S* wave ray path and therefore integrating a time shift along the converted *S* wave ray path is more complete, and (3) the use of the tomographic models naturally provides smoothing of the *Pds* timing corrections. As expected, the resulting standard deviation of the *Pds* timing corrections calculated from the tomographic models (0.52 s) is less than the *Pds* standard deviation calculated from the teleseismic residuals (0.62 s). The magnitude of this underestimation can be calculated by subtracting the variance of the teleseismic *Pds* signal (0.39 s^2) from the variance of the *Pds* timing corrections (0.28 s^2). This 0.11 s^2 of unaccounted for *Pds* timing variance

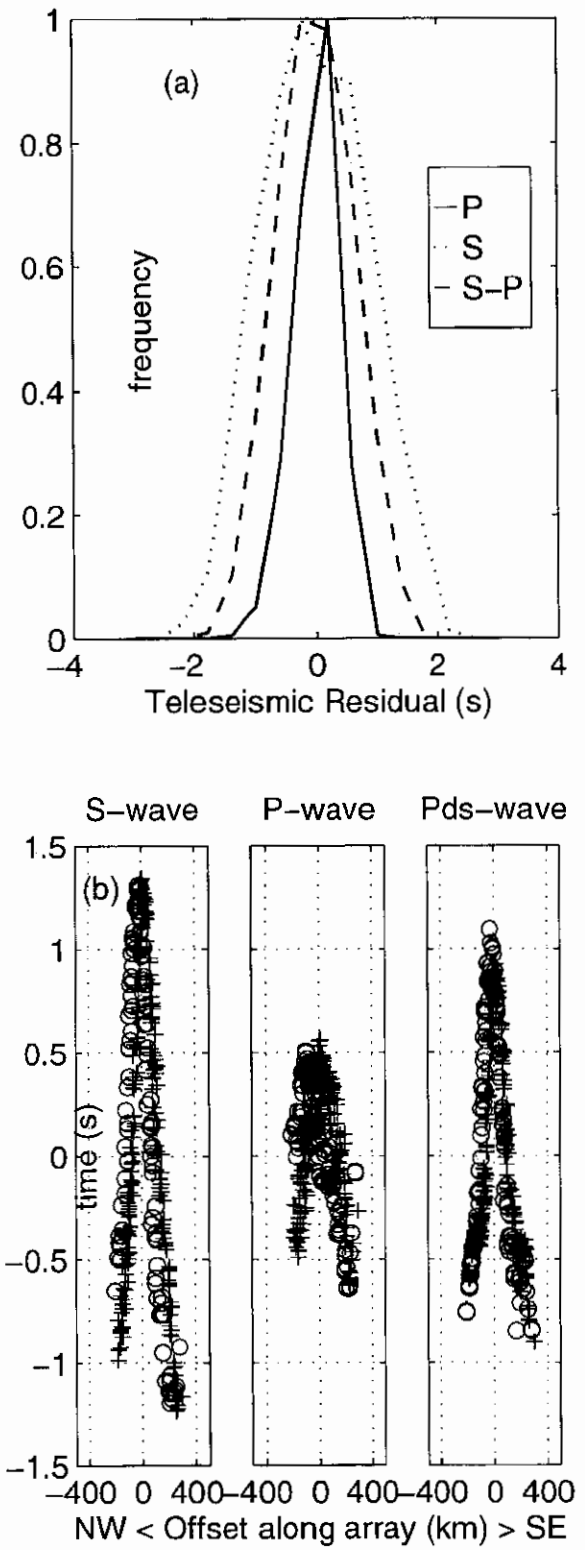

Figure 3. *Pds* timing corrections. (a) Histograms of the *P*, *S*, and *Pds* (*S-P*) timing corrections; the standard deviation of the three distributions is 0.37, 0.85, and 0.62 s, respectively. (b) The direct *P* and its associated converted *S* wave timing variations due to lateral heterogeneity are shown with respect to distance along the array. The *Pds* timing corrections applied are the difference between the *S* and *P* times which is labeled as the *Pds* wave. Note the simple pattern of relatively late arrivals which shifts slightly between the NW (crosses) and SE (circles) back azimuths.

suggests that up to ±0.66 s of unaccounted for timing variations due to lateral heterogeneity remains in the *Pds* ray set (i.e., up to ±7-km of apparent discontinuity topography).

Moveout Corrections

Timing variations associated with the different source-receiver separations are needed to effectively stack the data. Ideally, the moveout corrections would be calculated by ray tracing through three-dimensional velocity models of the shear and compressional velocity structure. In practice, the moveout corrections are predicted accurately by assuming a one-dimensional reference model $V_S(z)$ and a constant velocity ratio $R_v = V_p/V_S$. Reasonable changes in these velocity models produce less than a second of variation in the shape of the moveout curves. Thus for the 5- to 10-s dominant signal periods used herein, the quality of our moveout corrections is relatively insensitive to the assumed velocity models. Different velocity models can change the absolute depth to which an arrival is mapped; however, we do not interpret the absolute depths but focus on the relative discontinuity topography.

Given a one-dimensional reference model $V_S(z)$, a velocity ratio $R_v = V_p/V_S$, and a vertically incident *P* wave, the timing of an S wave converted at a depth D beneath a station, relative to the *P* wave arrival, in a flat Earth is [*Gurrola et al.*, 1994]

$$\Delta T_{ps0}(D,\ V_S(z),\ R_v) = \int_D^0 \frac{1}{V_S(z)} - \frac{1}{R_v V_S(z)}\,dz. \qquad (1)$$

Using the western U.S. model TNA [*Grand and Helmberger*, 1984] modified to have a 44-km-thick crust and an average upper mantle R_v of 1.82 from PREM [*Dziewonski and Anderson*, 1981], the vertically incident *Pds* arrival times for the 410- and 660-km discontinuities are 43 s and 67 s, respectively. Based on this velocity model, a 10-km variation in the depth to an upper mantle discontinuity will produce 1-s timing variation of the converted *S* wave. Our absolute discontinuity depths are conditionally dependent on the accuracy of our assumed reference model. While it is difficult to quantify the applicability of the TNA model to our region of study, inspection of a variety of western U.S. velocity models [e.g., *Julian and Anderson*, 1968; *Archambeau et al.*, 1969; *Masse et al.*, 1972; *Iyer and Hitchcock*, 1989] suggests that our absolute depths are accurate to within 10 km. The mean discontinuity depths of the 410-km (423 km) and 660-km (664 km) discontinuities found in the results section are within 15-km of the TNA model depths.

Generalizing the above normal incidence equation to an arbitrary incoming *P* wave angle of incidence produces [*Gurrola et a.*, 1994]

$$\Delta T_{ps}\left(p, V_s(z), R_v\right) = \int_D^0 \sqrt{1 - p^2 V_s^2(z)} - \sqrt{R_v^{-2} - p^2 V_s^2(z)}\ dz\ , \qquad (2)$$

where p is the ray parameter of the direct *P* wave. In a one-dimensional Earth, the actual ray parameter associated with our deepest converted phase (*P660s*) is predicted to vary by only 1.5% (i.e., the theoretical ray parameter of *P660s* is only 0.001 s/km smaller than the 0.06 s/km ray parameter of a 60° *P* wave). The magnitude of the moveout corrections changes with both the depth to an interface and the ray parameter of the incoming *P* wave (Figure 4). For example, the timing difference between an earthquake at $\Delta = 30°$ ($p = 0.04$ s/km) and an earthquake at $\Delta = 90°$ ($p = 0.08$ s/km) amounts to 9 s at 660 km

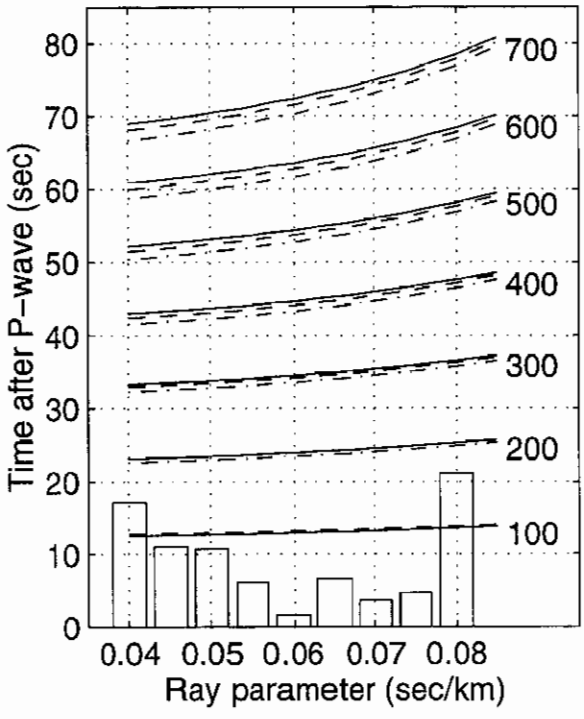

Figure 4. *Pds* moveout curves. The y axis is the relative time of a converted S wave arrival with respect to the P wave arrival calculated using equation (2), with labels to the right indicating the depth at which the P to S conversion occurs. The solid, dashed, and dashed-dotted curves are calculated using TNA with V_P/V_S 1.82, PREM with V_P/V_S of 1.82, and PREM with V_P/V_S of 1.78, respectively. At the bottom, a histogram of our ray parameter distribution is shown; the tallest histogram bin has 127 traces.

depth and 4 s at 410 km depth. A similar equation for the moveout curves associated with the $2p1s$ (two P legs, one S leg) reverberation have also been used to stack for reverberatory arrivals.

Summary of Processing

First, radial receiver functions are made from 423 teleseismic P wave arrivals. Second, the converted S wave ray set associated with the receiver functions (Figure 2) is geographically binned at our designated binning depths. Then the traces are band-pass filtered to either a 10-30 or 5-30 s band pass using a second-order zero-phase Butterworth filter. Next, when timing corrections are applied, the traces are split at 22 s (i.e., 200 km depth), and the *Pds* lateral heterogeneity timing corrections are used as shifts to the latter trace segment. This application of the timing shifts at 22 s is done because the application of timing statics to the beginning of the traces will result in incoherent stacking and hence amplitude reduction of the radial P wave. Finally, all the traces associated with each of the bins are stacked together along the moveout curves at 2-km increments in depth. For most of the plots the direct *Pds* moveout equation is used (equation (2)); however, for one plot, the $2p1s$ reverberation moveout equation is used. Plotting all the stack traces for each bin together makes the discontinuity image.

Results

Observation of *Pds* Moveout

The most robust characteristic used in *Pds* phase identification is observation of the correct moveout associated with a *Pds* wave [e.g., *Vinnik et al.*, 1996; *Paulssen*, 1988; *Bostock*, 1996]. This moveout can be directly observed by plotting all of our seismograms with respect to ray parameter (Figure 5). To smooth the image, the traces are binned into 0.001 wide ray parameter bins and an average trace is then formed for each bin. Plotting all these average traces together provides a direct view of the moveout characteristics of the data set. Inspection of this image shows that the $P660s$ arrival is the most coherent arrival and exhibits the expected moveout. The $P410s$ arrival also shows the expected moveout, although its smaller amplitude makes the image of the 410-km discontinuity appear less continuous. As will be discussed later, the energy arriving between 25 and 35 s is some combination of arrivals reverberated off discontinuities between 50 and 100 km depth and a candidate *Pds* arrival from a 300-km discontinuity. The arrival around 17 s is the mis-stacked Moho $2p1s$ reverberation.

Overlay Plots of NW and SE Back-Azimuth Events

To assess the consistency of the *Pds* arrivals, two images have been made using just the northwest and southeast back-azimuth *Pds* arrivals (Figure 6). After forming the image, an overlay plot of all the bins sampled by more than 30 traces is made and a mean trace calculated. Our most robust observation is that the transition zone thickness (i.e., 660 -410 km discontinuity depth) varies between 267 km in the NW back-azimuth stack to 234 km in the SE back-azimuth stack. Bearing in mind that the NW and SE back-azimuth arrivals have little overlap at a depth of 660 km (see Figure 2), this variation with back azimuth manifests differences in the transition zone thickness between the NW and SE halves of our transect. A small arrival around 510 km depth is seen in the SE stack but not in the NW stack. A strong arrival is observed in the 10-s images at 250 and 300 km depth in the NW and SE stacks. The most significant negative polarity arrival is the downswings which peak between 350 and 370 km depth in the 10-s stacks. (Note that the side-lobe amplitude measured from the radial P wave arrival is 24% of the central peak.)

Phasing Depth Analysis

A useful way to assess the origin of the arrivals observed in our images is to stack the data over a range of moveout curves or phasing depths [*Vinnik*, 1977]. The procedure consists of forming a series of discontinuity images in which the entire depth range of each image is stacked along the same moveout curve for a particular depth (Figure 7). If the arrivals from a discontinuity are indeed direct *Pds* arrivals, then one expects the discontinuity image to come into focus when the correct phasing depth is used. The success of this procedure is dependent on a uniform distribution of ray parameters contributing to any given bin. If there is not a relatively uniform distribution of ray parameters, then a discontinuity will stack with equivalent amplitudes at different phasing depths. In this case, the only effect will be offsets in the depth to which a discontinuity is migrated. The ray parameter distribution of the entire data set (Figure 4) shows a relatively uniform distribution; however, for individual bins along the edges of the image a relatively poor distribution exists. In addition, the sensitivity

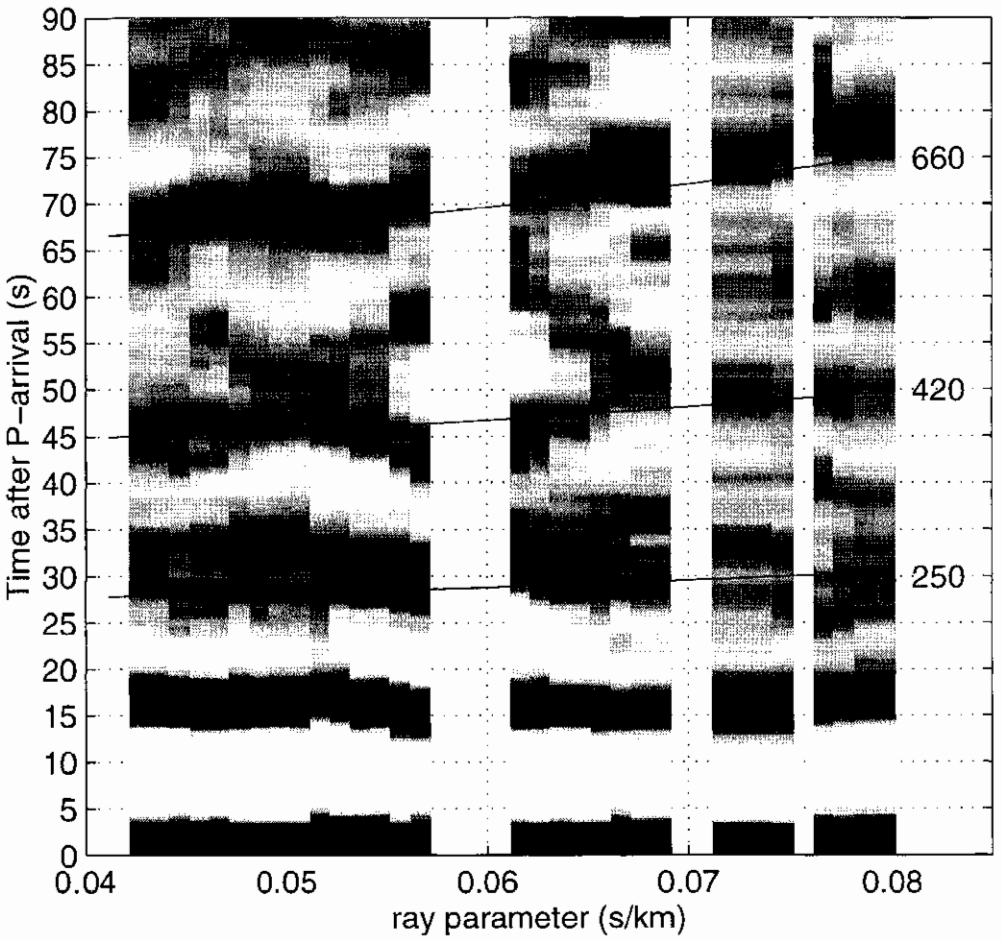

Figure 5. Ray parameter versus time after *P* wave. The entire *Pds* ray set was binned by ray parameter and mean traces formed for each bin. Plotting all these summary traces together forms the image. Black and white shading represents ±0.05% amplitude of the radial *P* wave. The moveout curves (same curves as in Figure 4) for the indicated discontinuity depths have been plotted. The *P*660*s* and *P*410*s* phases are the most prominent discontinuity phases. The 2*p*1*s* Moho reverberation arrives at 15-20 s, and the energy between 25 and 35 s is the combination of energy reverberated from 50- to 100-km lithospheric discontinuities and perhaps some direct arriving *Pds* energy from 250- to 300-km discontinuity structure.

of the discontinuity image to different phasing depths varies as a function of depth. For example, the 200-km depth *Pds* moveout curve has only 2 s of variation, whereas the 700-km depth curve has 9 s of variation (Figure 4). Therefore given the 5- and 10-s dominant period of our signal, there is little phasing depth resolution present above 200 km depth. Inspection of the phased images shows that the 410- and 660-km discontinuities come into focus at the nominal depths of 400 and 700 km, respectively (Figure 7). The focusing of these discontinuities is evidenced by the increase in lateral continuity and amplitude of the 410- and 660-km discontinuities when the discontinuities are phased correctly.

Discontinuity Structure Above 410 km and Reverberation Analysis

To assess the discontinuity structure above 300 km depth, a set of images focused on this region were made in the 5- to 30-s band pass (Figure 8). In Figure 8a, an image was made with the following characteristics: the binning depth was placed at 50 km, and no timing corrections were applied. Inspection of this image shows that the Moho varies between 40 and 45 km depth. The most significant variation in the Moho is a 5-km thickening of the crust beneath the YHT. Arrivals between the Moho and 100-km are observed, with the most continuous arrival being a positive amplitude arrival beneath the middle two thirds of the array at a depth of about 75 km.

Given the observation of a positive amplitude "discontinuity" arrival around 75 km, a 2*p*1*s* reverberation from this discontinuity will be falsely migrated (using the *Pds* moveout equation) to a depth of about 240 km. To assess the likelihood that arrivals around this depth range are 2*p*1*s* reverberations, we compare images constructed by stacking along the direct *Pds* (Figure 8b) and 2*p*1*s* moveout curves (Figure 8c). These two images are made with the binning depth at 250 km. In addition, timing corrections are applied to the direct *Pds* image but are not applied to the 2*p*1*s* image (because we are trying to isolate shallow reverberations in the 2*p*1*s* image). Note that the Moho 2*p*1*s* reverberation and energy around 250 km depth SE of the hinge line stacks with higher amplitudes when the 2*p*1*s* reverberation moveout curves are used (Figure 8c). Northwest of an offset of 200 km, the direct *Pds* image shows an arrival at 220 km, but this is most likely a side lobe of the negative polarity Moho 2*s*1*p* re-

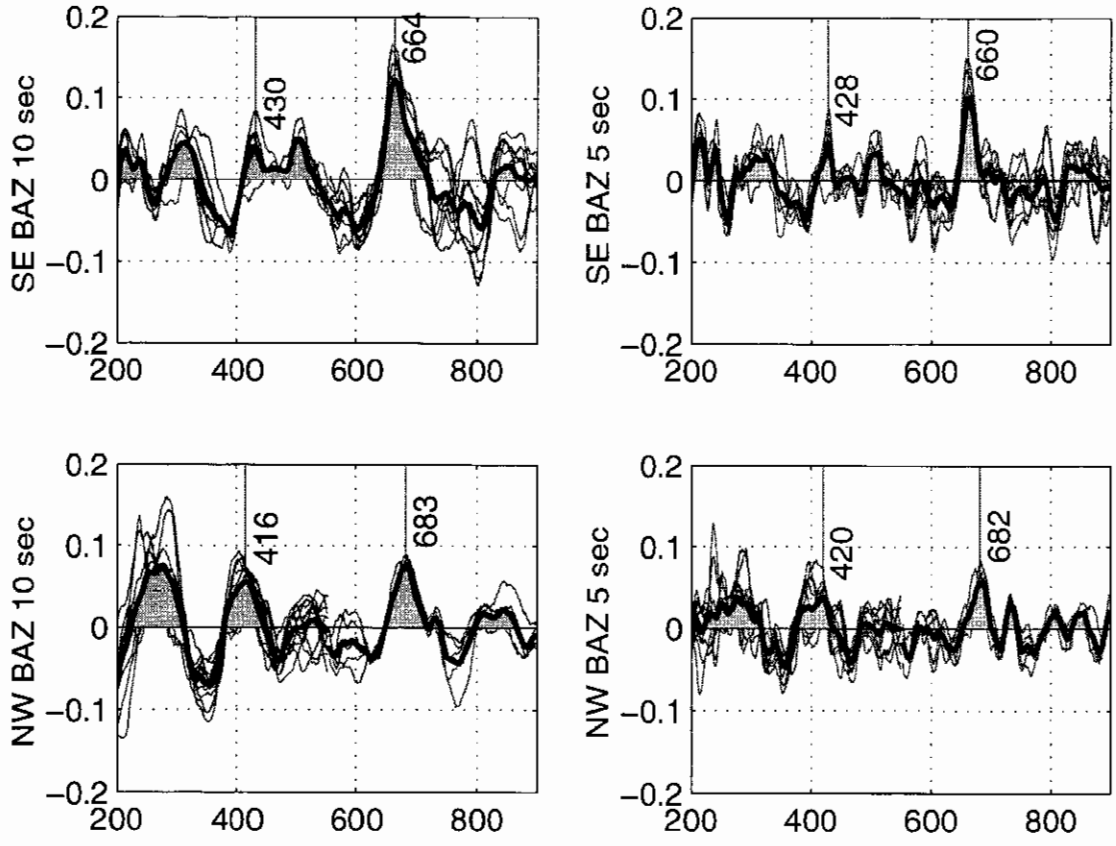

Figure 6. Overlay plots. To assess the consistency of the observed arrivals, two images were made using *Pds* rays from only NW (left two graphs) and SE (right two graphs) back azimuths for the 5- and 10-s dominant periods labeled. Thin lines are individual bin traces with more than 30 traces in the bin; the thick line is the mean of the thin lines. The numbers to the right of the traces are the depths of the 410- and 660-km discontinuities. Note that the transition zone thickness from the 10-s NW and SE back-azimuth stacks are 267 (683-416 km) and 234 km (664-430 km), respectively.

verberation. The best candidate for a direct *Pds* arrival is the arrival at about 290 km beneath the middle third of the image. However, the reverberation image shows that these 290-km arrivals stack with similar amplitudes along the $2p1s$ moveout curves. Thus at this point it is difficult to know whether or not a discontinuity resides at 290 km depth. Future work using *S* to *P* conversion (which do not have reverberations arriving in this time window) will be needed to further investigate this depth range.

410- and 660-km Discontinuities

In Figure 9, images focused on the 410- and 660-km discontinuities structure are constructed. The image of the upper 570 km was constructed using a binning depth at 400 km, whereas the image below 570 km was constructed using a binning depth at 700 km. The Moho arrival and its associated $2p1s$ (upswing) and $2s1p$ (downswing) reverberations are observed at the depths of 40-45, 150, and 180 km, respectively, in the 5-s image. The Moho reverberations have been falsely migrated (migration performed using *Pds* moveout) and stack coherently because there is only 1- to 2-s difference between the direct arrival and retrograde moveout curves for such a shallow interface. In the 5- and 10-s images, the largest and most laterally continuous arrivals are from the 660- and 410-km discontinuities. In both images, it appears that the 410-km discontinuity is offset to 390-km SE of the hinge line of the western U.S. rift margin. However, we believe that the 390-km arrival could be a falsely migrated reverberation from a discontinuity around 120 km depth. Furthermore, close inspection of the 5-s image shows that a small-amplitude arrival at 425 km depth resides beneath the 390-km arrival. Beneath the NW margin of the YHT, the 410-km discontinuity is upwarped to its shallowest depth (410 km). To the SE of this upwarp, the 410-km discontinuity dips downward toward the hinge line to its deepest depth at 435 km. In the 10-s image, the 660-km discontinuity is imaged as our highest-amplitude and most laterally coherent discontinuity. The most well-resolved aspects of the 660-km discontinuity are the flat segment in the southeast third of the image and the 25-km downwarp beneath the northwest third of the image. In the 5-s image, the 660-km discontinuity is clearly imaged except in a 200-km-wide zone beneath the YHT. Here the 660-km discontinuity is imaged as a set of smaller-amplitude arrivals at both 660 and 620 km depth. At the southeast end of the array the 660 is flanked by arrivals at depths of 590 and 710 km in the 5-s image. However, the poor ray sampling in this region will allow reverberations to stack coherently; thus these arrivals may be reverberations from shallower discontinuities.

Correlation of 410 and 660 Topography

To assess the effect of our *Pds* timing corrections, a series of images have been formed in which the amplitude of the timing

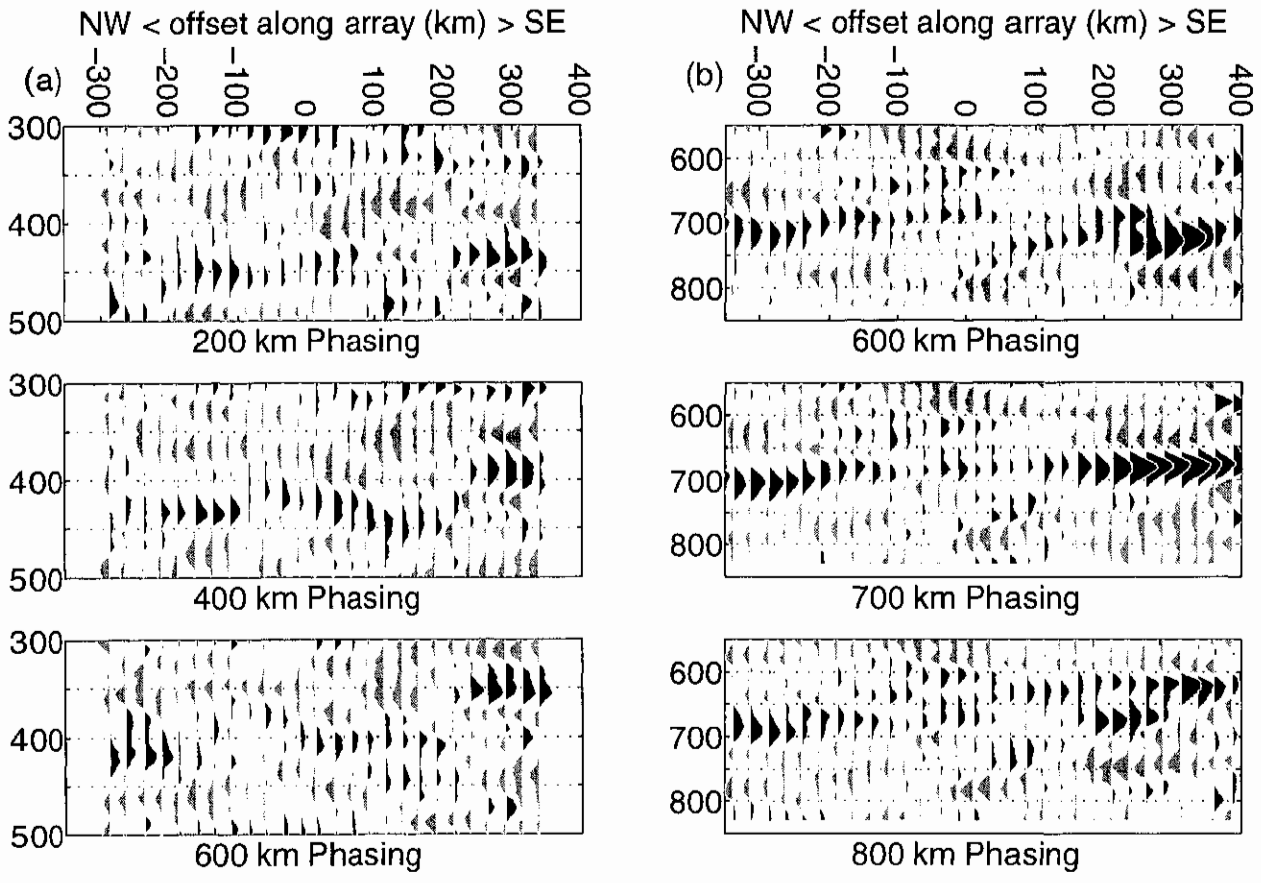

Figure 7. Phasing depth images. To assess whether the discontinuities come into focus when the correct moveout corrections are applied, phasing depth images are shown. Positive and negative polarity energy is plotted in black and gray, respectively. The radial *P* wave is used as a reference amplitude level, and the spacing between each individual trace is 10% of the radial *P* wave. (a) Focusing of the image of the 410-km discontinuity at 400-km phasing depth. Note that because there is little ray parameter variation for the bins between 200- and 330-km offset, these arrivals are simply shifted in depth with little change is pulse shape. (b) Focusing of the image of the 660-km discontinuity at 700-km phasing depth.

corrections have been globally rescaled. This is done by forming three separate images using no *Pds* time corrections, the normal time corrections (Figure 3b), and twice the normal time corrections. As an example of the effect of the timing correction, we present a 5-s image with no timing corrections (Figure 9c). Comparison of Figures 9b and 9c shows that the discontinuity topography is flattened in some regions and enhanced in others by application of the timing corrections. The expected effect of the timing corrections applied can be estimated by comparing the binning of the *Pds* ray set shown in Figure 2 with the patterns of the travel time corrections shown in Figure 3b. The effect of these timing corrections on the images is evidenced by the slight flattening of the two 660 "downwarps" (i.e., depressed 660-km discontinuity at offsets between -200 and -400 km) as the magnitude of the time corrections is changed from zero (Figure 9c) to normal (Figure 9b). Note that the image of the 410-km discontinuity is made more continuous and the sharp offsets flattened by application of the timing corrections.

To quantify the degree of correlation between the 660- and 410-km discontinuity topography, the depth of the largest positive arrival around these depths has been picked (Figure 10). If our *Pds* timing was dominated by unaccounted for *Pds* timing variations associated with lateral velocity heterogeneity (as opposed to being dominated by the timing shifts imparted by discontinuity topography), then one expects the topography on the 410- and 660-km discontinuity to be correlated [e.g., *Stammler et al.*, 1992; *Bostock*, 1996]. Inspection of Figure 10 shows that the 410 and 660 topography does not appear to be either positively or negatively correlated. For example, in the NW half of the array, the 410-km discontinuity is flat, while the 660-km discontinuity is bowed downward by 25 km. Likewise, in the SE half of the array, the 410-km discontinuity shows 25 km of topography, whereas the 660-km discontinuity is flat. Of course the 600-km length of our profile means that we have no ability to assess the style of correlation for discontinuity topography with wavelengths greater than the 600-km fundamental period of our sampling.

Noise Sensitivity

In assessing noise sensitivity, the hypothesis being tested is whether a given arrival in a stack results from a direct *P* to *S* conversion from the underlying mantle or from stacking noise. Sources of noise present on the seismograms include both random background Earth noise and signal-generated noise (e.g.,

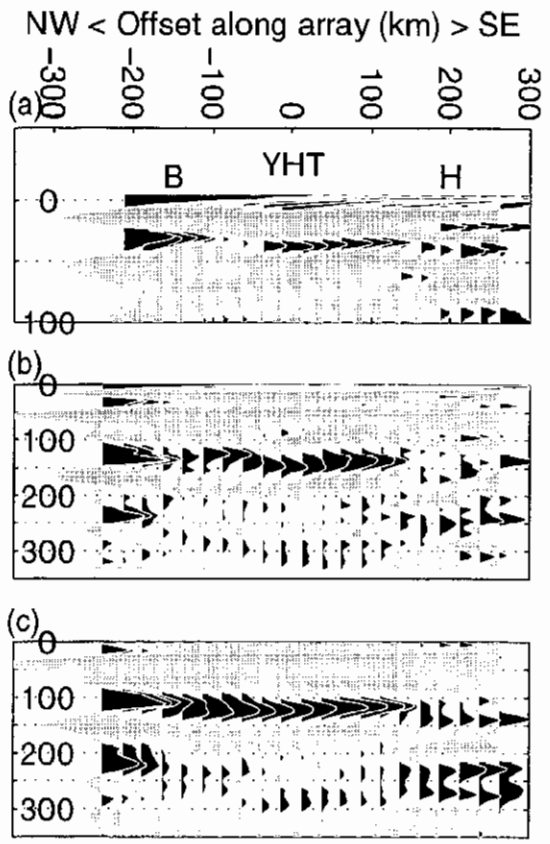

Figure 8. Comparison of direct versus $2p1s$ reverberation images. Positive and negative polarity energy is plotted in black and gray, respectively. The radial P wave is used as a reference amplitude level, and the spacing between each individual trace is 10% of the radial P wave. (a) Construction by stacking along the direct Pds moveout curves with the binning depth at 50-km. Note the Moho and positive arrivals around 80-km depth. (b) Stacking using the direct Pds moveout curves with the binning depth at 250-km. (c) The same as Figure 8b except that stacking was performed along the $2p1s$ moveout curves. To facilitate comparison, time was mapped to depth the same as in Figure 8b by using equation (1). Note that the Moho $2p1s$ reverberation stacks more coherently in the $2p1s$ image. Comparison of Figures 8b and 8c shows that the arrivals between 280 and 300 km stack equally well along the direct Pds and $2p1s$ moveout curves.

reverberations when direct Pds arrivals are being isolated, P-Rg topographic scattering [*Clauser and Langston*, 1995], and complex P-SV resonances in low-velocity surface layers [*Levander and Hill*, 1985]). Sources of processing noise include unaccounted for lateral velocity heterogeneity and variations in the ray parameter and the converted S wave pulse shape by discontinuity topography induced multipathing [*van der Lee et al.*, 1994]. We have performed the following tests to investigate the contribution of noise to our discontinuity images:

1. To investigate the a posteriori distribution functions of the stack traces, we use the bootstrap resampling technique [*Efron and Tibshitani*, 1986]. One hundred realizations of each stack trace are calculated by random resampling (with replacement) of the receiver functions contributing to a bin. Histograms are then calculated from these realizations at every point (i.e., depth) along each stack trace. Inspection of these histograms shows that the distributions are generally bell shaped, so that the mean and standard deviation estimates resulting from these distributions provide reasonable estimates of a stack trace and its error. The standard deviation of the stack traces (not the smaller standard errors) calculated from the bootstrap resampling are typically 1-2% of the radial P wave amplitude.

2. The depth of the binning plane and bin width constrains the tradeoff between the statistical and spatial resolution of our images. Because the ray set diverges with depth, the 700-km binning depth results in an approximate 25% reduction in the number of rays per bin with respect to the 400-km binning depth. Wider bins allow the capture of more rays per bin; however, this also results in more spatial averaging. To address the effect of these parameters, we have stacked and inspected the images through a wide range of binning depth and bin widths. These tests show that while details do change, the discontinuity features we interpret are robust.

3. To assess scattering and the presence of nonplanar discontinuity structure, the tangential receiver functions are stacked in the same manner as the radial receiver functions. This shows that the average tangential amplitudes are half of the radial amplitudes and that the lateral coherence of the tangential arrivals is significantly less than that of the radial arrivals. Some coherent tangential energy is observed, which is consistent with the large discontinuity topography imaged with the radial receiver functions (Figure 9).

4. The noise preceding the radial P wave is processed in the same way as the postevent signal to assess the coherence which results from our processing. This is done by processing the 100 s preceding the P wave in the same fashion that we have processed the 100 s after the P wave. Stacking of the noise preceding the P wave produces an average peak amplitude which is 4% of the radial P wave. The spatial overlap of neighboring bins produces lateral coherence over distances of three stack traces (i.e., 75 km). The amplitudes and coherence of the noise stacks are substantially less than observed in the true images.

5. Randomized midpoint stacks (Figure 11) are compared with true midpoint stacks (Figure 9). If discontinuity structure is planar, then the randomization of midpoints should not affect the images outside of statistical fluctuations associated with variations in data quality. However, if more than 20-km of relief exists on a discontinuity, then the associated Pds timing shifts (i.e., >2 s) produced by such relief will result in incoherent stacking and hence degradation of the discontinuity images. Pds timing corrections are applied before the randomization so that this source of stack incoherence is removed. The result of this experiment shows that the 410- and 660-km discontinuity arrivals are visible as bands of positive arrivals; however, the lateral coherence of these discontinuities is significantly less than the correct midpoint images (Figure 9). This loss of stack coherence associated with the randomization of the midpoints is strong evidence supporting the finding of true discontinuity topography in the correct midpoint stacks.

Discussion

From a global perspective, the effects of lateral velocity heterogeneity above 410 km depth appear to dominate the 5-s global variation in $P660s$ and $P410s$ phases as suggested by the correlation of $P410s$ and $P660s$ times [*Stammler et al.*,

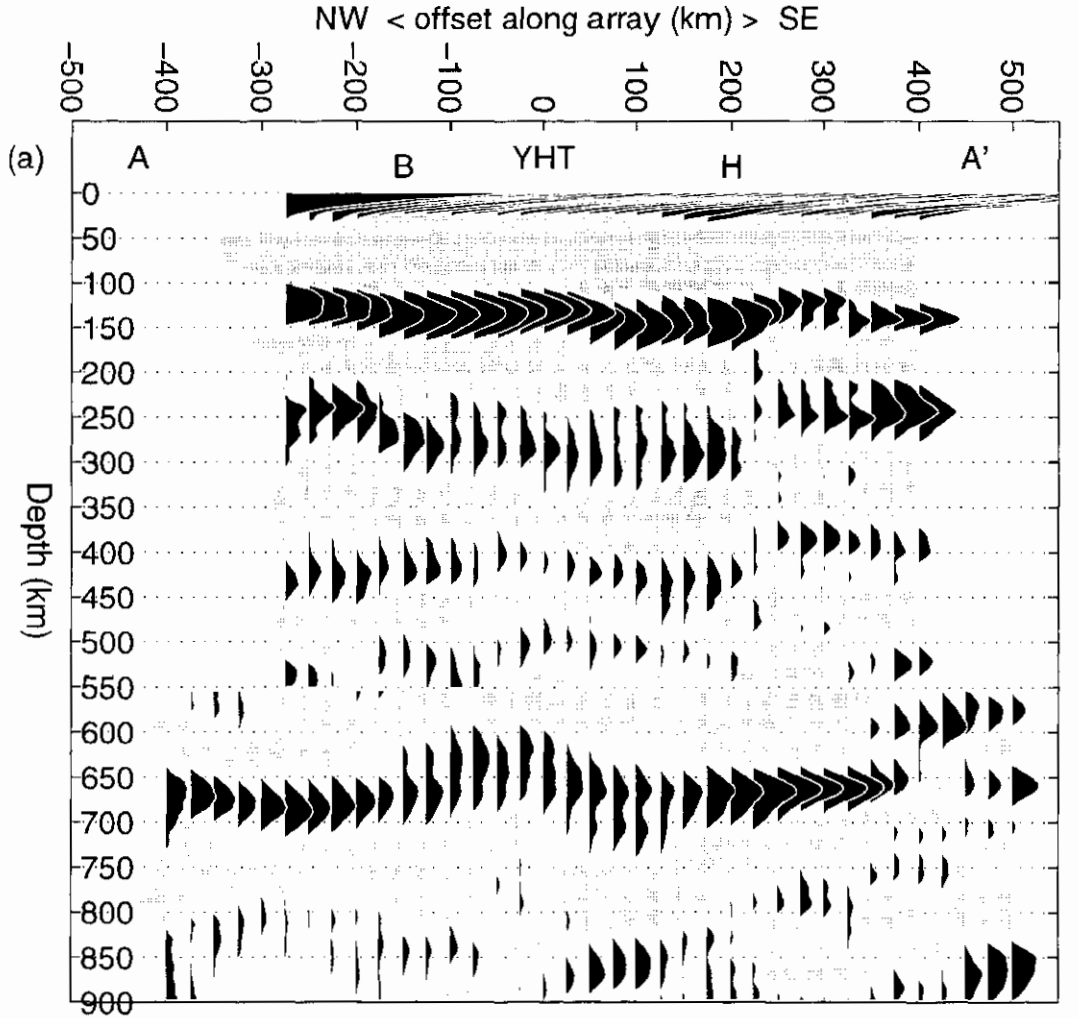

Figure 9. Discontinuity images. Positive and negative polarity energy is plotted in black and gray, respectively. The radial *P* wave is used as a reference amplitude level, and the spacing between each individual trace is 10% of the radial *P* wave. (a) Band-pass image at 10-30 s, called 10-s, image. (b) band-pass image at 5-30 s, called 5-s image. (c) Image at 5 s with no timing corrections applied.

1992; *Bostock*, 1996]. Thus researchers have focused interest on measuring the transit time of *Pds* waves through the transition zone by simply measuring the differential time between *P*660*s* and *P*410*s* arrivals. This provides a relatively robust estimate of the transition zone thickness which is relatively insensitive to velocity heterogeneity above the 410-km discontinuity. In addition, if the velocity heterogeneity in the transition zone is relatively small (i.e., less than 3% average shear wave velocity variations throughout the transition zone), then *Pds* travel time variations due to transition zone velocity heterogeneity will be less than 1 s (i.e., 10 km of variation in the transition zone thickness).

Recent studies find that the range of transition zone timing (i.e., *P*660*s* minus *P*410*s* arrival times) is less than 2 s, which is much less that the 5-s range in *P*660*s* and *P*410*s* times observed globally [*Stammler et al.*, 1992; *Bostock*, 1996; *Vinnik et al.*, 1996]. Given that a *Pds* phase travels about 10 km/s through the transition zone, the implication is that less than 20 km of transition zone thickness variation exists. If these thickness variations derive from vertically coherent transition zone thermal anomalies, then the opposite Clapeyron slopes present at the 410- and 660-km discontinuities predicts the occurrence of anticorrelated discontinuity topography [*Revenaugh and Jordan*, 1991b; *Bostock*, 1996]. If this scenario is true, then a 20-km variation in transition zone thickness requires only a 125° thermal anomaly. However, if vertically coherent thermal anomalies are not present, then larger temperature anomalies are required. An alternate scenario is a situation in which one discontinuity is unperturbed and thus all the transition zone thickness variation must derive exclusively from topography on the other boundary. In this case, the required thermal anomaly would be about twice that of the anticorrelated case (i.e., 250°).

Given that these previous *Pds* studies were global in scope and presumably captured the complete range of transition zone thickness variations present on the planet, our finding of 35 km of transition zone thickness variation beneath a 600-km-long transect is somewhat surprising. While it is possible that our transect has serendipitously sampled some uniquely heterogeneous transition zone mantle, a simpler explanation is that our processing technique simply permits lateral variations in transition zone thickness to be more accurately imaged. We note that the above cited estimates of relatively small transition zone thickness variations results from either single-

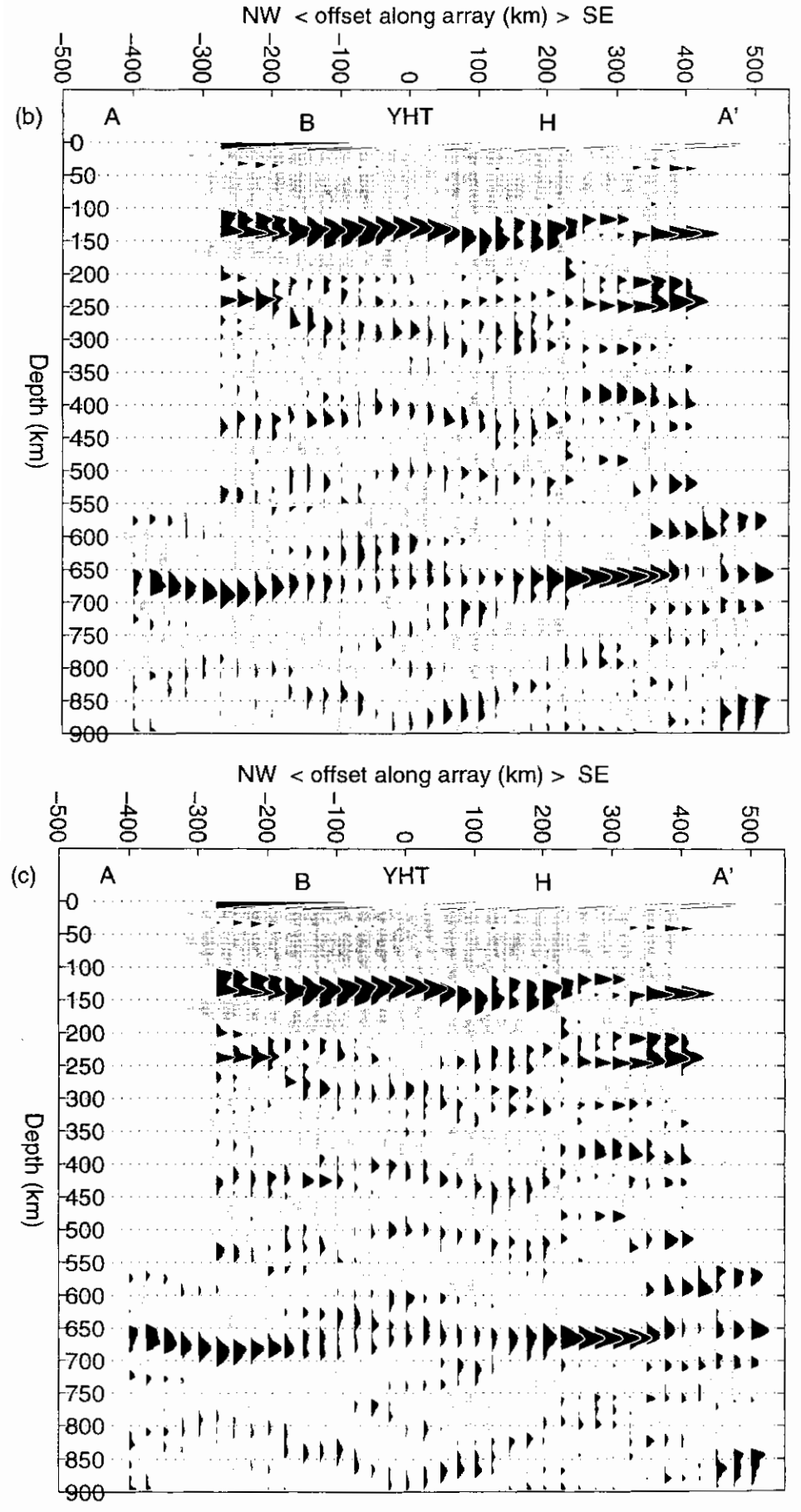

Figure 9. (continued)

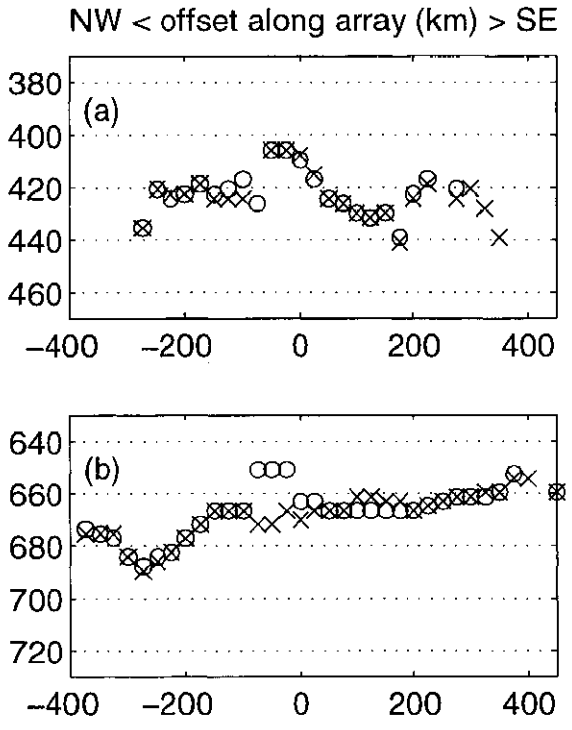

Figure 10. Discontinuity depths at 410 and 660 km. To assess discontinuity depth variations, the largest arrival greater than 2% of the radial *P* wave is found between (a) 390 and 460 km depth and (b) 640 and 700 km depth. Crosses are picked from the 5-s image, and circles are picked from the 10-s image. The symbol size is proportional to the arrival amplitude. A conservative fit to the observed topography is drawn to assess the magnitude and degree of correlation of the discontinuity topography. The 410-km discontinuity varies between 415 and 435 km, and the 660-km discontinuity varies between 660 and 685 km. This 660/410 topography results in 35 km of variation in the transition zone thickness. No obvious correlation of the 410- and 660-km discontinuity topography is apparent.

station and/or widely spaced multiple-station stacks. In both cases, a large area of the 410- and 660-km discontinuities is sampled (see Figure 2), and hence small amounts of discontinuity topography will be coherently averaged together. However, if >20 km of discontinuity topography is present, then the resulting >2-s variations in *Pds* arrival times will cause incoherent stacking (as demonstrated in Figure 11). Thus while these single-station and/or widely spaced multiple-station stacks can provide robust averages, there may be a bias in the previous *Pds* work to not "see" larger variations in transition zone thickness.

An important result of this study is the finding of an uncorrelated 410- and 660-km discontinuity structure with up to 30 km of topography over 100- to 300-km scale lengths. Of course, the style of discontinuity topography correlation for spatial wavelengths greater than the 600 km length of our profile are not interrogated. We note that the defocusing effects predicted by this scale of discontinuity topography is consistent with synthetic seismogram experiments which seek to explain the intermittent visibility of 410- and 660-km discontinuity arrivals [e.g., *Neele and Sneider*, 1992; *van der Lee et al.*, 1994]. If these scales of discontinuity undulations are indeed a pervasive feature, the implication is that 100- to 300-km wavelength temperature anomalies of the order of 250° linger around the 410- and 660-km discontinuities. However, at these short scale lengths, our findings of an undulatory 410- and 660-km discontinuity structure may not dominantly reflect the thermal structure of the mantle. Indeed, velocity gradients associated with phase transformations of the garnet-pyroxene component of the mantle [*Anderson*, 1989], chemical layering [*Anderson*, 1989], variations in mantle hydration [*Wood*, 1996], and kinetic effects [*Solamatov and Stevenson*, 1994] have all been suggested as sources of discontinuity topography.

Given that the origin of hotspot volcanism still remains an open question, it is worthwhile for us to address what light this study may shed on the origin of the Yellowstone volcano-tectonic system. The sheared plume model for the origin of the YHT [*Smith and Braile*, 1994] suggests that a mantle plume currently rises beneath the Yellowstone caldera, which is 250 km to the NE of our transect (Figure 1). The plume is predicted to have passed beneath our line array around 6-7 m.y. ago [*Smith and Braile*, 1994], coincident with the huge caldera eruptions at this time. Thus unless plume material has remained ponded at the 410- and/or 660-km discontinuities since 6-7 m.y. ago, no thermal anomaly is predicted at the 410- and 660-km discontinuities beneath our line. However, the sheared plume model does predict that a layer of warm plume material should reside beneath our line to a depth of 150-200 km [*Smith and Braile*, 1994].

The most visually apparent correlation between the surface trace of the YHT and its discontinuity structure is the shallowing of the 410-km discontinuity beneath the NW margin of the YHT and its deepening toward the hinge line (Figures 10 and 12). However, if this discontinuity topography results from thermal variations, then the warmest mantle residing at 410 km depth exists not beneath the YHT, but 150 km to the SE near the western U.S. hinge line. The lack of warm mantle at 410 km depth beneath the YHT is consistent with the tomographic images which require no velocity perturbations below 250-km depth to satisfy the travel times residuals [*Schutt et al.*, 1995; *Saltzer and Humphreys*, 1997]. Thus given our current tomographic resolution, there is no reason to believe that the low-velocity blob beneath the YHT (Figure 12) extends into the transition zone. As was discussed in the preceding paragraph, any possible mantle plume should reside not beneath our transect, but beneath the Yellowstone caldera (Figure 1). Thus if a plume is not perturbing the thermal structure present at 410 km depth, then what is? We suggest that (1) much of this short-wavelength discontinuity topography may not dominantly manifest thermal variations and (2) the transition from the actively convecting mantle beneath the Basin and Range Province to the convectively isolated mantle beneath the Wyoming Province may be associated with deep seated thermal and chemical variations. In addition, if a large rheologic contrast exists across the hinge line, this will strongly control upper mantle flow patterns associated with the SW absolute motion of the North American plate and any flow driven locally by thermal and/or chemical contrasts beneath our line.

In the 10-s image, the 660-km discontinuity appears upwarped beneath the NW margin of the YHT, although this visual observation is somewhat misleading. In the more spatially resolved 5-s image (Figure 9b), the 660-km discontinuity is not upwarped; instead, an additional arrival at 620 km is observed. Thus it is the close proximity of the 620- and 660-

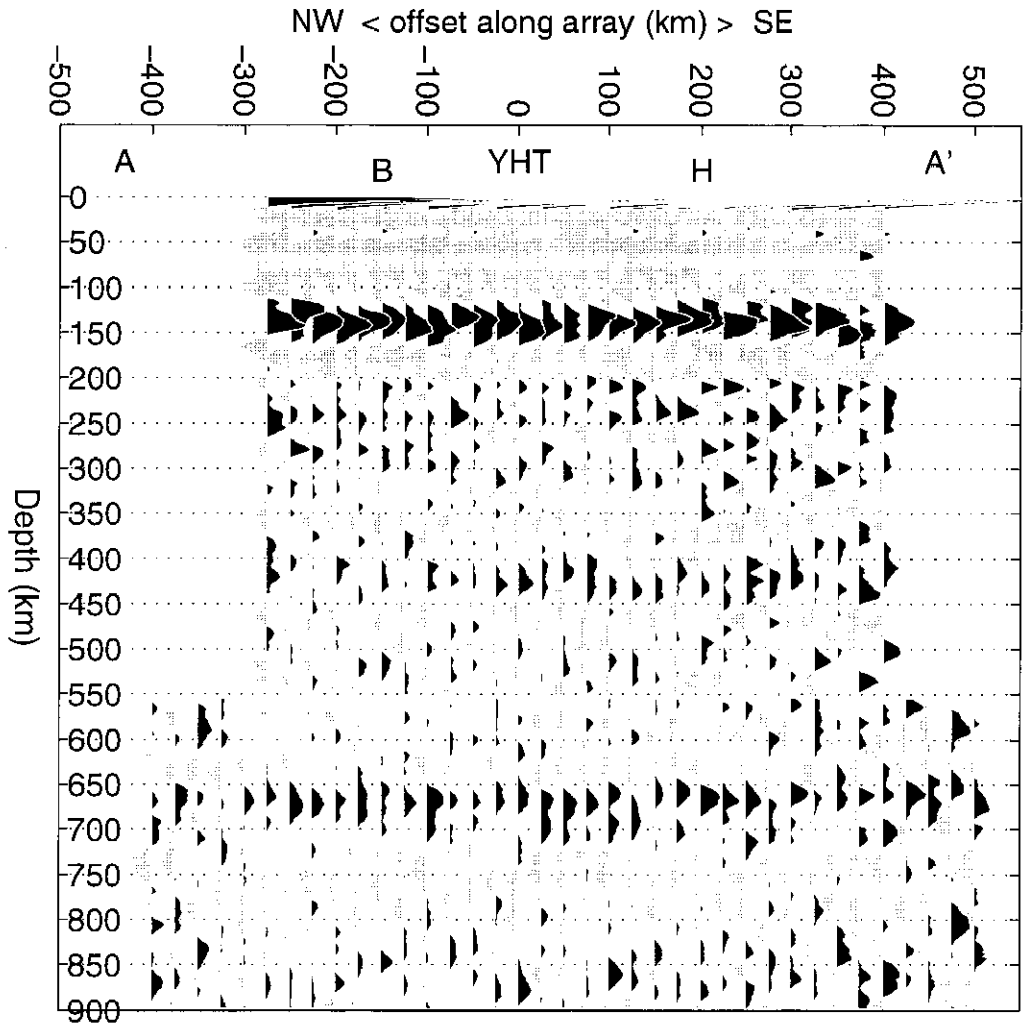

Figure 11. Randomized midpoint image for 5- to 30-s band pass. Plotting parameters are the same as Figure 9. To assess the change in lateral coherence of the discontinuities, the data are stacked in the same manner as the discontinuity images (Figure 9), except that the *Pds* rays contributing to a bin are randomly chosen. The distribution of rays per bin is kept the same as in the true images, and *Pds* timing corrections are applied before midpoint randomization. Comparison of this image with the correctly binned discontinuity image (Figure 9b) shows a large decrease in discontinuity amplitude and continuity. We suggest that this results from the midpoint randomization which produces a situation in which the 20-30 km of 410- and 660-km discontinuity topography found in this paper is randomly averaged together, causing stack incoherence.

km discontinuity arrivals which creates the appearance of an upwarp in the 10-s image. This region of the 660 km discontinuity is well sampled, and thus there is no reason to suspect that noise is producing an artifact discontinuity at 620 km depth. Three-dimensional variations in discontinuity structure perpendicular to the YHT could produce artifacts in our two-dimensional stacking plane. However, our sampling perpendicular to the stacking plane is confined to a relatively narrow 80-km-wide swath (Figure 1). Thus it seems that a complex 660-km discontinuity structure is observed beneath the NW margin of the YHT. The most robust 660-km discontinuity topography observed is the downward deflection of the 660-km discontinuity NW of the YHT. If this is thermal topography, then relatively cool mantle is required here. Given that slab fragments have recently been imaged in the transition zone beneath the western U.S. [*van der Lee and Nolet*, 1997], we speculate that this downwarp could be a fragment of slab lying on the 660-km discontinuity. A slab was presumably subducting in this region 40 m.y. ago as evidenced by the Challis volcanic arc present at the NW end of our transect.

Conclusion

Lateral variations in the discontinuity structure have been imaged by common midpoint style processing of radial receiver functions produced from a temporary deployment of PASSCAL broad band stations across the Yellowstone hotspot track. This processing of seismograms greatly improves the quality of the stacks over single-station stacks because signal-generated noise which is coherent at a single-station becomes incoherent in multistation stacks. Our most robust finding is that the transition zone thickness varies by 30-35 km. This variation in transition zone thickness occurs over a 300-km lateral scale length and results from 20-30 km of to-

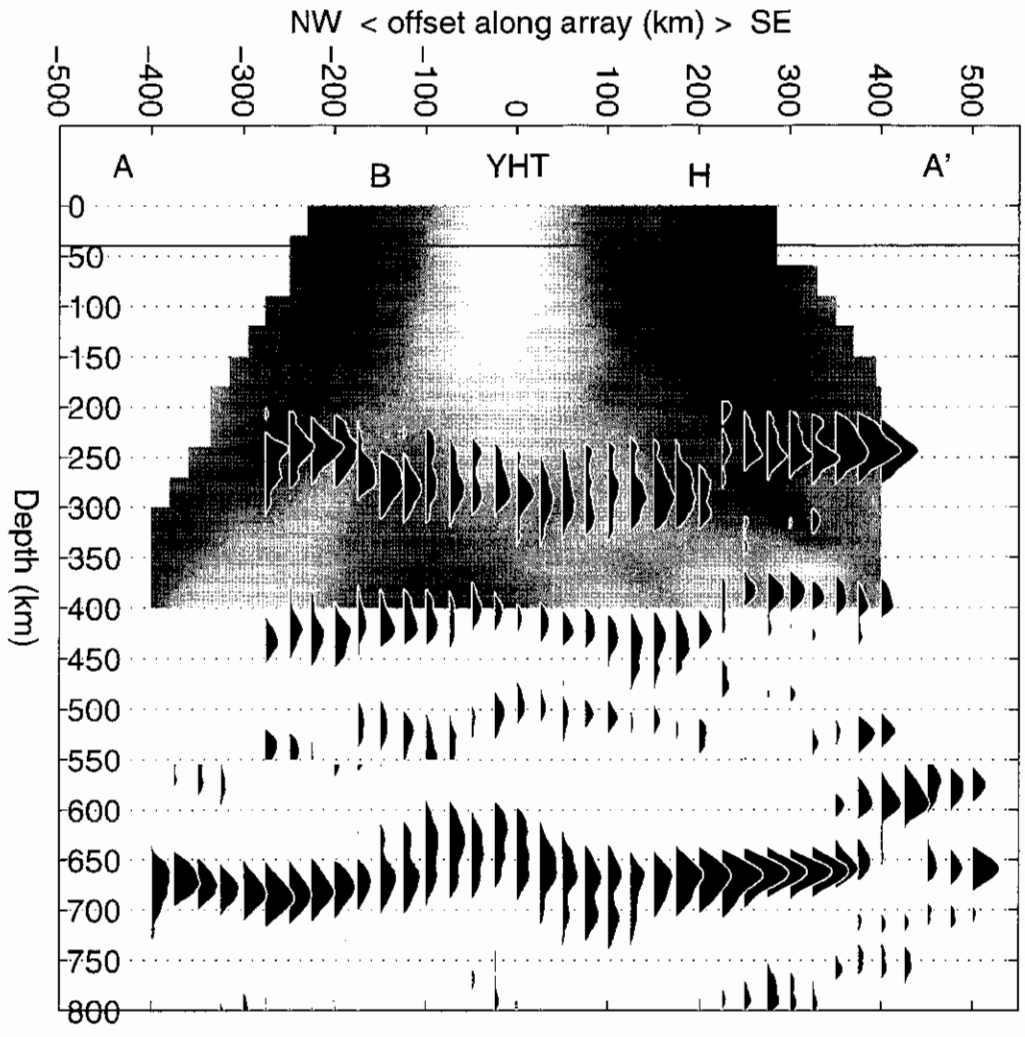

Figure 12. Ten-second discontinuity image and YHT *S* wave velocity structure [*Schutt et al.*, 1995]. The white and black shading are slow and fast velocities, respectively, which vary by 6%. Only the positive polarity energy from our 10-s image is plotted (Figure 9a).

pography on the 410- and 660-km discontinuities. Comparison of the topography on the 410- and 660-km discontinuities shows that this topography is not positively correlated, as would be expected if unaccounted for lateral velocity heterogeneity dominated the timing of the *P*410*s* and *P*660*s* phases. Furthermore, the topography on the 410- and 660-km discontinuities is not negatively correlated as would be expected if the discontinuity topography on these phase boundaries was controlled exclusively by vertically coherent thermal variations throughout the transition zone. If a thermal origin for the topography observed on the 410- and 660-km discontinuities is assumed, then 250° temperature anomalies would be required to produce the discontinuity topography we report. However, at the short lateral scale lengths observed by this study, other processes may also create significant topography on the 410- and 660-km discontinuities. To assess these other processes, further work will be required to assess the amplitude and sharpness characteristics of the discontinuities. In addition, the velocity heterogeneity present at the 410- and 660-km discontinuities needs to be resolved to within 1%, so that the thermal hypothesis for the origin of this discontinuity topography may be formally tested. Unfortunately, our current tomographic velocity models do not yet provide this level of accuracy. However, significant improvements in the quality of our velocity and discontinuity images is expected after the deployment of a 45-station PASSCAL line in 1997, which will extend this work 450 km to the SE into central Colorado.

Acknowledgments. This research was funded by NSF grants EAR-9405542 and EAR-9319008. The quality of the paper was improved by comments by associate editor Peter Shearer, Justin Revenaugh, and an anonymous reviewer. We thank Rebecca Saltzer, Derek Schutt, and Gene Humphreys for allowing use of their velocity models.

References

Anderson, D. L., *Theory of the Earth*, Elsevier Sci., New York, 1989.

Anderson, D. L., and C. Sammis, Partial melting in the upper mantle, *Phys. Earth Planet. Inter.*, *3*, 41-50, 1970.

Archambeau, C. B., E. A. Flinn, and D. G. Lambert, Fine structure of the upper mantle, *J. Geophys. Res.*, *74*, 5825-5865, 1969.

Baumgardt, D. R., and S. S. Alexander, Structure of the mantle beneath Montana LASA from analysis of long-period, mode-converted phases, *Bull. Seismol. Soc. Am.*, *74*, 1683-1702, 1984.

Bina, C. R., and G. Helffrich, Phase transition Clapeyron slopes and transition zone seismic discontinuity topography, *J. Geophys. Res.*, *99*, 15853-15860, 1994.

Bostock, M. G., *Ps* conversions from the upper mantle transition zone beneath the Canadian landmass, *J. Geophys. Res.*, *101*, 8393-8402, 1996.

Clauser, R. H., and C. A. Langston, Modeling *P-Rg* conversions from isolated topographic features near the NORESS array, *Bull. Seismol. Soc. Am.*, *85*, 859-873, 1995.

Clayton, R. W., and R. A. Wiggins, Source shape estimation and deconvolution of teleseismic body waves, *Geophys. J. R. Astron. Soc.*, *47*, 151-177, 1976.

Dziewonski, A. M., and D. L. Anderson, Preliminary reference Earth model, *Phys. Earth Planet. Inter.*, 25, 297-356, 1981.

Efron, B., and R. Tibshitani, Bootstrap methods for standard errors, confidence intervals, and other measures of statistical accuracy, *Stat. Sci.*, *1*, 54-77, 1986.

Gaherty, J. B., and T. J. Jordan, Lehmann discontinuity as the base of an anisotropic mechanical boundary layer beneath continents, *Science*, *268*, 1468-1471, 1995.

Grand, S. P., and D. Helmberger, Upper mantle shear structure of North America, *Geophys. J. Int.*, *76*, 399-438, 1984.

Green, R. W., and A. L. Hales, The travel times of *P* waves to 30° in the central United States and upper mantle structure, *Bull. Seismol. Soc. Am.*, *58*, 267-290, 1968.

Gurrola, H., J. B. Minster, and T. Owens, The use of velocity spectrum for stacking receiver functions and imaging upper mantle discontinuities, *Geophys. J. Int.*, *117*, 427-440, 1994.

Hales, A. L., A seismic discontinuity in the lithosphere, *Earth Planet. Inter.*, *11*, 109-118, 1969.

Hales, A. L., Upper mantle models and the thickness of the continental lithosphere, *Geophys. J. Int.*, *105*, 355-363, 1991.

Iyer, H. M., and T. Hitchcock, Upper-mantle velocity structure in the continental U.S. and Canada, *Mem. Geol. Soc. Am.*, *172*, 681-710, 1989.

Jordan, T. H., Structure and formation of the continental tectosphere, in *Oceanic and Continental Lithosphere: Similarities and Differences*, edited by M. A. Menzies and K. G. Cox, *J. Petrol.*, Special Volume, 11-37, 1988.

Julian, B. R., and D. L. Anderson, Travel times, apparent velocities and amplitudes of body waves, *Bull. Seismol. Soc. Am.*, *58*, 339-366, 1968.

Kawakatsu, H., and F. Niu, Seismic evidence for a 920-km discontinuity in the mantle, *Nature*, *371*, 301-305, 1994.

Langston, C. A., Corvallis, Oregon, crustal and upper mantle receiver structure from teleseismic *P* and *S* waves, *Bull. Seismol. Soc. Am*, *67*, 713-724, 1977.

Lehmann, I., On the travel times of *P* as determined from nuclear explosions, *Bull. Seismol. Soc. Am.*, *54*, 123-139, 1964.

Levander, A. R., and N. R. Hill, *P-SV* resonances in irregular low-velocity surface layers, *Bull. Seismol. Soc. Am.*, *75*, 847-864, 1985.

Leven, J. H., I. Jackson, and A. E. Ringwood, Upper mantle anisotropy and lithospheric decoupling, *Nature*, *289*, 234-239, 1981.

Masse, R. P., M. Landisman, and J. B. Jenkins, An investigation of the upper mantle compressional velocity distribution beneath the Basin and Range province, *Geophys. J. R. Astron. Soc.*, *30*, 19-36, 1972.

Moores, E. M., Southwest U.S.-East Antarctic (SWEAT) connection: A hypothesis, *Geology*, *19*, 425-428, 1991.

Neele, F., and R. Sneider, Topography of the 400-km discontinuity from observations of long-period P400P phases, *Geophys. J. Int.*, *109*, 670-682, 1992.

Nolet, G., S. P. Grand, and B. L. Kennett, Seismic heterogeneity in the upper mantle, *J. Geophys. Res.*, *99*, 23753-23766, 1995.

Paulssen, H., Evidence for a sharp 670-km discontinuity as inferred from P to S converted waves, *J. Geophys. Res.*, *93*, 10489-10500, 1988.

Priestley, K. F., J. Cipar, A. Egorkin, and N. Pavlenkova, Upper mantle velocity structure beneath the Siberian platform, *Geophys. J. Int.*, *118*, 369-378, 1994.

Revenaugh, J. S., and T. H. Jordan, Mantle layering from *ScS* reverberations; 3, The upper mantle, *J. Geophys. Res.*, *96*, 19781-19810, 1991a.

Revenaugh, J. S., and T. H. Jordan, Mantle layering from *ScS* reverberations; 2, The transition zone, *J. Geophys. Res.*, *96*, 19763-19780, 1991b.

Revenaugh, J. S., and S. A. Sipkin, Mantle discontinuity structure beneath China, *J. Geophys. Res.*, *99*, 21911-21927, 1994.

Ritsema, J., M. Hagerty, and T. Lay, Comparison of broadband and short-period seismic waveform stacks: Implications for upper-mantle discontinuity structure, *Geophys. Res. Lett.*, *22*, 3151-3154, 1995.

Rodgers, D. W., W. R. Hackett, and H. Ore, Extension of the Yellowstone plateau, eastern Snake River Plain, and Owyhee plateau, *Geology*, *18*, 1138-1141, 1990.

Saltzer, R., and E. D. Humphreys, Upper mantle *P* wave velocity structure of the eastern Snake River Plain and its relationship to geodynamic models of the region, *J. Geophys. Res.*, in press, 1997.

Schmeling, H., and G. Bussod, Variable viscosity convection and partial melting in the continental asthenosphere, *J. Geophys. Res.*, *101*, 5411-5423, 1996.

Schutt, D., E. D. Humphreys, and K. D. Dueker, Tomographic inversion of teleseismic S waves across the track of the Yellowstone hotspot (abstract), *EOS Trans. AGU*, *76*, 412, 1995.

Shearer, P. M., Constraints on upper mantle discontinuities from observations of long-period reflected and converted phases, *J. Geophys. Res.*, *96*, 18147-18182, 1991.

Shearer, P. M., Transition zone velocity gradients and the 520-km discontinuity, *J. Geophys. Re.*, *101*, 3053-3066, 1996.

Smith, R. B., and L. W. Braile, The Yellowstone hotspot, *J. Volcanol. Geotherm. Res.*, *61*, 121-187, 1994.

Solomatov, S., and D. J. Stevenson, Can sharp seismic discontinuities be caused by non-equilibrium phase transformations?, *Earth Planet. Sci. Lett.*, *125*, 267-279, 1994.

Stammler, K., R. Kind, N. Petersen, G. Kosarev, L. Vinnik, and L. Qiyuan, The upper mantle discontinuities: Correlated or anticorrelated, *Geophys. Res. Lett.*, *19*, 1563-1566, 1992.

Stunff, Y. L., C. W. Wicks, and B. Romanowicz, *P'P'* precursors under Africa: Evidence for mid-mantle reflectors, *Science*, *270*, 74-77, 1995.

Tackley, P. J., and D. J. Stevenson, A mechanism for spontaneous self-perpetuating volcanism on the terrestrial planets, in *Flow and Creep in the Solar System: Observation, Modeling and Theory*, pp. 307-321, Kluwer Acad., Norwell, Mass., 1993.

van der Lee, S., and G. Nolet, Seismic image of the trailing edge of the Farallon plate, *Nature*, in press, 1997.

van der Lee, S., H. Paulssen, and G. Nolet, Variability of *P660s* phases as a consequence of topography of the 660 km discontinuity, *Phys. Earth Planet. Inter.*, *86*, 147-164, 1994.

Vidale, J. E., and H. M. Benz, Upper mantle seismic discontinuities and the thermal structure of subduction zones, *Nature*, *356*, 678-683, 1992.

Vinnik, L. P., Detection of waves converted from *P* to *SV* in the mantle, *Phy. Earth Planet. Inter.*, *15*, 39-45, 1977.

Vinnik, L. P., R. A. Avetisjan, and N. G. Mikhailova, Heterogeneities in the mantle transition zone from observations of *P*-to-*SV* converted waves, *Phys. Earth Planet. Inter.*, *33*, 149-163, 1983.

Vinnik, L. P., G. Kosarev, and N. Petersen, Mantle transition zone beneath Eurasia, *Geophys. Res. Lett.*, 23, 1485-1488, 1996.

Wood, B. J., The effect of H_2O on the 410-kilometer seismic discontinuity, *Science*, *268*, 74-76, 1995.

K. G. Dueker and A. F. Sheehan, Campus Box 216, CERES, University of Colorado, Boulder, Boulder, CO 80309. (e-mail: ken@mantle.colorado.edu)

(Received April 8, 1996; revised December 3, 1996;
accepted December 9, 1996.)